2020

# Electrodynamics Modeling of Plasmonic-Organic Hybrid Waveguides

Marcus Michel


Senior Thesis in Physics

# Electrodynamics Modeling of Plasmonic-Organic Hybrid Waveguides

*Author:*
Marcus Michel

*Advisor:*
Dr. Gordon Stecklein
*External Readers:*
Dr. Lewis Johnson
Dr. David Masiello

Submitted to Pomona College in Partial Fulfillment
of the Degree of Bachelor of Arts

January 23, 2020

# Contents

## Acknowledgements

I would like to thank:

Professor Gordon Stecklein, my thesis advisor, for his constant support throughout the semester. Being able to talk through and clarify physical concepts with him was incredibly helpful, and his regular feedback about each chapter's structure was invaluable for creating this thesis.

Dr. Lewis Johnson, my research advisor over the summer, for his guidance and mentorship. His regular check-ins informed the direction of my research and solidified my understanding of the material. I am especially grateful for him taking part in the process of editing this thesis and for making the trip down to Claremont to hear my final presentation.

Professors David Masiello and Bruce Robinson for welcoming me into their groups and funding my research this summer. Their feedback and guidance was indispensable.

Elliot Beutler and Jake Busche, graduate students in the Masiello group, for being such amazing mentors over the summer, patiently bringing me up to speed on the fundamentals of their work. Elliot allowed me to build off of his custom scripts for creating and visualizing the target geometry, along with his MatLab code for creating magnitude and vector field electric field plots.

Dr. Xiang-Tian Kong for bringing the issue with DDA's periodic boundary conditions to my attention.

The members of both the Robinson and Masiello groups for so generously offering me their time and expertise.

Derek Pickell and Katheryn Kornegay for reading and editing my thesis over the course of the semester.

This work was supported by the Air Force Office of Scientific Research (FA9550-19-1-0069), the University of Washington Student Technology Fund, and the University of Washington.

**Abstract**

Optical fibers have multiple advantages over conventional electrical connections, such as lower energy losses and higher bandwidth. To use optics for chip-to-chip communication, electro-optic (EO) modulators need to be scaled down to be incorporated on integrated circuits. This size reduction has been accomplished using plasmonic-organic hybrid (POH) waveguides, which make use of nonlinear organic EO materials and surface plasmon polaritons to achieve light modulation in devices with lengths on the micron scale. As these devices are just starting to be developed, there are many avenues for their potential optimization. In order to streamline and reduce the cost of the optimization process, a computational model of these devices is being developed. Using this model, researchers will be able to experiment with varying device parameters, such as geometry, material composition, and cladding layers and see how device performance is affected in order to inform the fabrication of actual test devices. This thesis explores the Discrete Dipole Approximation (DDA) as a potential software for this computational model. To do so, a simplified model of a POH waveguide was created to validate whether or not DDA produces physically expected results. Four separate simulations using this simplified model produce results that are consistent with physical expectations. Additional simulations can provide further confirmation of these initial results.

# Chapter 1

# Introduction

## 1.1 Electro-Optic Modulators

In this age of mass data transmission and with the increasing demand for higher bandwidth, higher efficiency communications, the advantages of fiber optics over traditional electrical communications have become apparent. Already, fiber-optic cables transport optical signals with low energy losses and large bandwidth [1], and the electro-optic (EO) modulators that convert electrical data to optical signals are also efficient. However, to take advantage of the benefits of optical signals for chip-to-chip communication, these EO modulators must become much smaller than they currently are. Specifically, they must be compatible with transistors on an integrated circuit in both size and voltage. Silicon-organic modulators and plasmonic modulators have been shown to have lengths of 100's of microns and 10's of microns respectively. These plasmonic modulators are what the Robinson group at the University of Washington and their collaborators at ETH Zurich are concerned with. The following sections will go over the general structure of the modulators and discuss the mechanisms through which they work, as well as the challenges associated with scaling them down, wrapping up with an overview of what this specific project, creating a computational model of these devices, is meant to accomplish.

## 1.2 Pockels Effect

The specific method of EO modulation that the devices these groups are concerned with make use of the Pockels effect, where electrically polarizable materials demonstrate a change of index of refraction when an electric field is applied to them. Figure 1.1 shows the general structure of a Mach-Zehnder interferometer, which is a specific device architecture used in these groups:

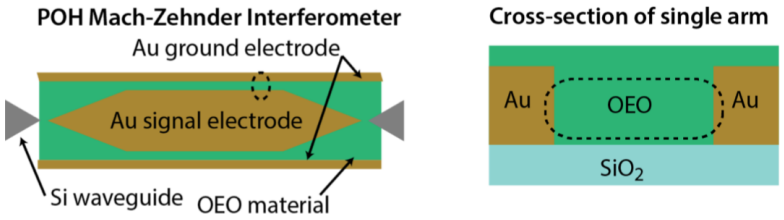


**Figure 1.1:** Graphic from Johnson et al. [2]. Left: A top view of a Mach-Zehnder Interferometer. The green is a dielectric material (in this case, an organic polymer), the strips of gold are the outer rails, the central gold slab is the center island at which the electric signal is applied, and the gray triangles are tapered silicon mode converters, which are necessary for coupling in the light to the surface plasmon polariton as discussed in the following section. Right: Vertical cross section of a single arm of the interferometer, as indicated by the dotted oval on the left diagram. The organic electro-optic (OEO) material in between the gold rail and center island exhibits the Pockels effect.

This device architecture is utilized for its simplicity, which allows for easier testing of different material parameters. Mach Zehnder interferometers work by sending an optical frequency signal (single-mode fiber optics commonly use light with wavelengths of 1310 nm and 1550 nm, which correspond to frequencies of $2.29 * 10^{14}$ Hz and $1.94 * 10^{14}$ Hz, respectively) through each arm of the interferometer. These arms are called waveguides; they guide and confine the electromagnetic wave through mechanisms which vary with each type of waveguide. The following section describes a few options for waveguides and the advantages of each.

The change in index of refraction due to an induced voltage of U is

$$\Delta n = r_{33} n^3 U/(2w_{gap}) \tag{1.1}$$

where $r_{33}$ is the electro-optic coefficient, n is the index of refraction, and $w_{gap}$ is the width of the slot. [3]

When the phases of the waves in the two arms of the interferometer are shifted relative to each other by $\pi$ radians, or 180 degrees, they will be exactly out of phase when they recombine at the other end of the interferometer, resulting in destructive interference and an output signal with amplitude 0 as shown in figure 1.2.

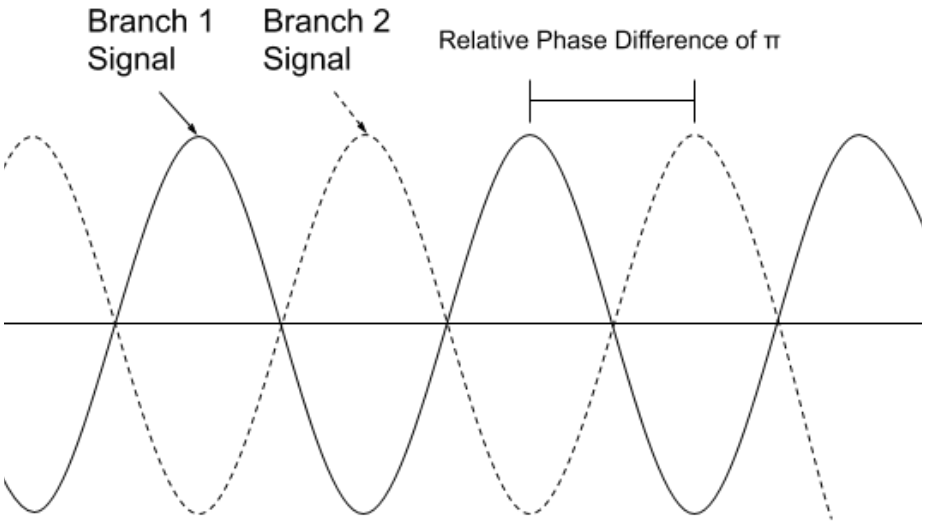


**Figure 1.2:** Relative phase difference of $\pi$ of the optical signal in the two arms of the Mach-Zehnder interferometer, resulting in destructive interference at the far end of the interferometer.

This is the requirement for digital signal processing: the ability to rapidly shift a signal between 1 (on) and 0 (off). Figure 1.3 shows how phase information is encoded on the light wave in a single arm of the interferometer. The figure shows a phase change of a half wavelength, whereas the shift needed for the MZI design in figure 1.1 is a quarter wavelength, as the two arms add up to a relative phase of half a wavelength.

As optical frequency waves travel down each arm of the interferometer, an oscillating radio frequency voltage is applied to the center island. The radio frequency voltage is the electrical signal that is being converted into an optical

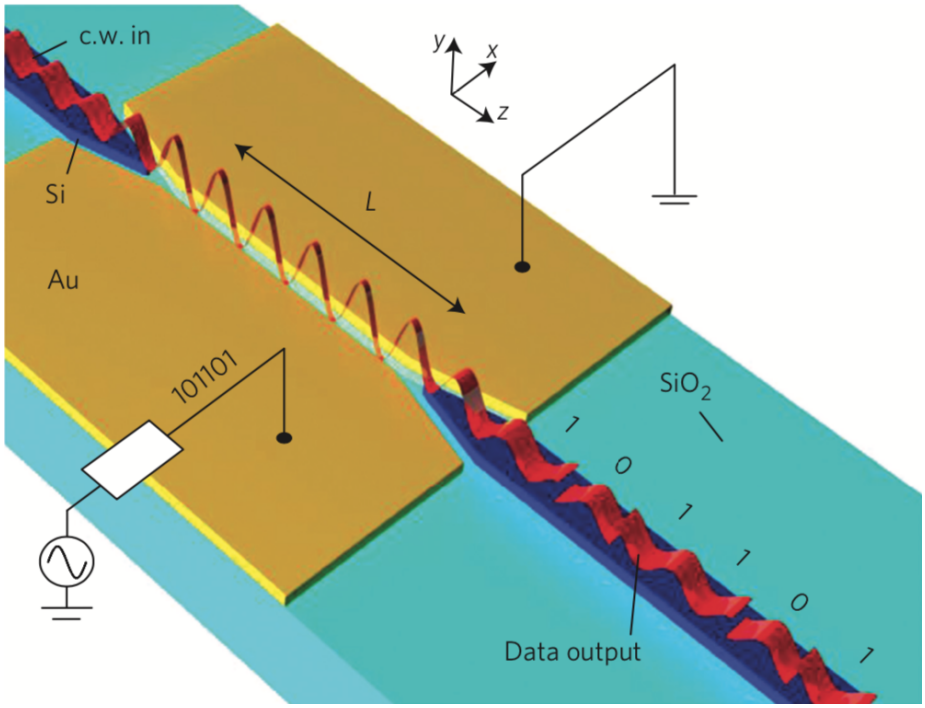


**Figure 1.3:** Graphic of a single plasmonic phase modulator from Melikyan et al. [3]. A continuous optical frequency wave (incoming from the left side) is coupled into the surface plasmon polariton (SPP, discussed in following section) with a tapered silicon tip. The phase of this SPP is modulated with an alternating (radio frequency) voltage input signal, as indicated by the overlaid circuit diagram graphics.

signal. The voltage creates an electric field across each arm of the interferometer, and these electric fields change the index of refraction of the material inside each waveguide. This in turn shifts the phase of light forward if the index is increased, or backward if the index is decreased as shown in figure 1.4.

As the same electrical signal is being applied to the center island, the phase of the light in each arm will be shifted in opposite directions relative to each other. Thus, the devices can be half as long compared to devices in which only one arm is exposed to the signal.

To recap, an optical signal is split and sent down both arms of the interferometer. Those signals propagate at different rates through each arm due to the

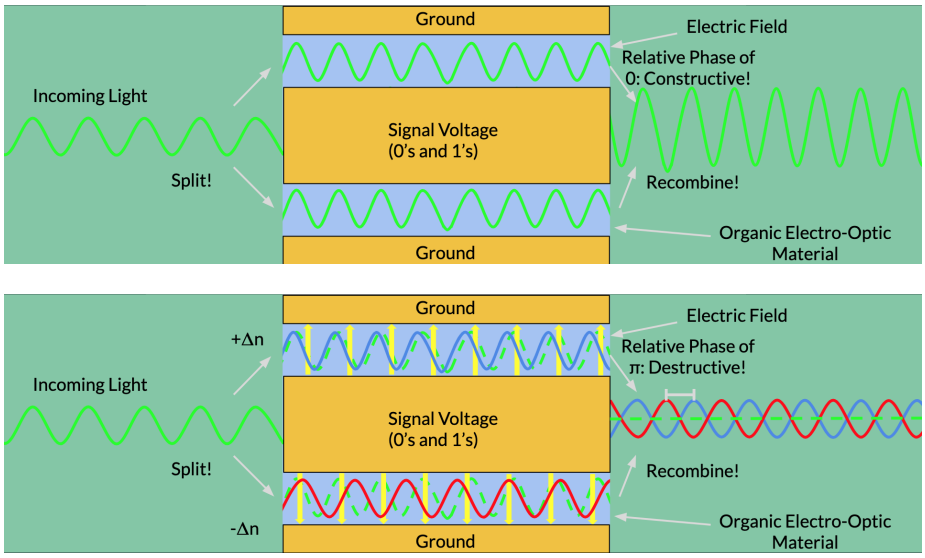


**Figure 1.4:** Graphics showing light being split into the arms of the MZI. The top image is when no voltage is being applied to the center island, therefore the waves recombine constructively. The bottom image shows the shifting of wavelengths due to the applied electric field, and the destructive recombination at the other end of the interferometer.

Pockels effect. The change in index of refraction is caused by a radio frequency input voltage, which is therefore changing the signals' relative phase. When the light is recombined at the other end of the MZI, their relative phase determines the amplitude of the output light signal. Constructive interference is a 1, and destructive interference is a 0.

Note that with this set up, an applied voltage results in a 0 in the optical signal, and no applied voltage results in a 1 in the optical signal. This means the electrical and optical signals are exact opposites. To remedy this, it is possible to have one arm of the interferometer a half wavelength longer than the other, so when no voltage is applied the output optical signal is 0, as would be expected. This offset can also be accomplished by using arms of same size but slightly different widths.

## 1.3 Plasmonics

Electro-optic devices need to be scaled down while maintaining their efficiency to better meet the increasing needs of data communications.

Some waveguides make use of total internal reflectance in order to contain the wave–these are photonic waveguides. This is the same mechanism that allows for lossless data transmission in fiber optic cables, where a material of high index of refraction is surrounded by one of low index; the wave is perfectly reflected without energy losses. Both all-organic thin film devices and silicon-organic hybrid (SOH) devices make use of this purely photonic method of confinement, resulting in device lengths of 10s of millimeters and 100s of microns, respectively. For many applications, this size is acceptable. However, for dense integration of these modulators on an integrated chip scale. Implementing these modulators on the integrated chip scale would allow for optical communication between chips, thereby reducing energy consumption and increasing processing power [4]. Given that these modulators would be on the chip itself, it is crucial to reduce the device's footprint as much as possible to avoid taking up room that could be used for more transistors.

Certain EO modulators operate at or near plasmonic resonance in order to reduce device length. The use of plasmonics can accomplish this size reduction. In physics, a plasmon refers to the collective oscillation of electrical charge within a material, as seen in figure 1.5.

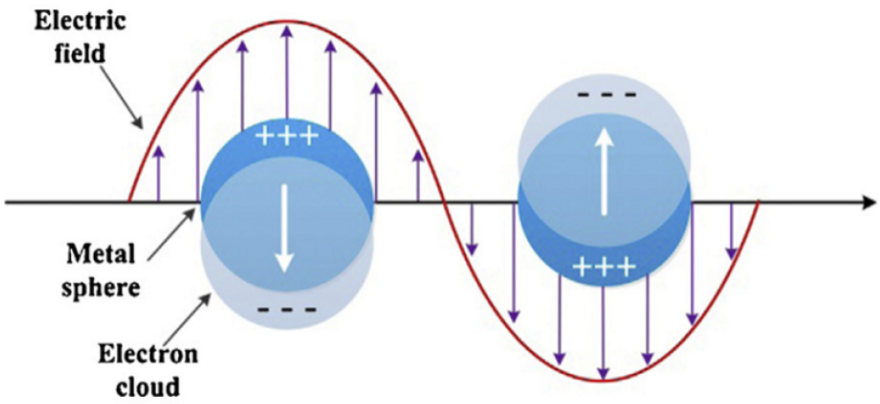


**Figure 1.5:** Depiction of the shift in electron cloud relative to the metal ions making up a sphere due to an applied electric field from Sun et al. [5]

As the applied electric field oscillates, so does the material's electron cloud. This oscillation is defined as a plasmon. When these plasmons are excited by light, which is made up of an oscillating electromagnetic field, they are referred to as plasmon polaritons. The word polariton refers to the coupled state between a photon and an elementary excitation, in this case a plasmon. [6]

Plasmonic waveguides use the excitation of a surface plasmon polariton (SPP), a surface wave that travels at the interface between a metal and a dielectric (insulator) [3]. This surface wave can be modulated using the Pockels Effect, much like with photonic devices. Figure 1.6 depicts the charge configurations associated with an SPP at a metal surface, and an SPP confined to a spherical nanoparticle.

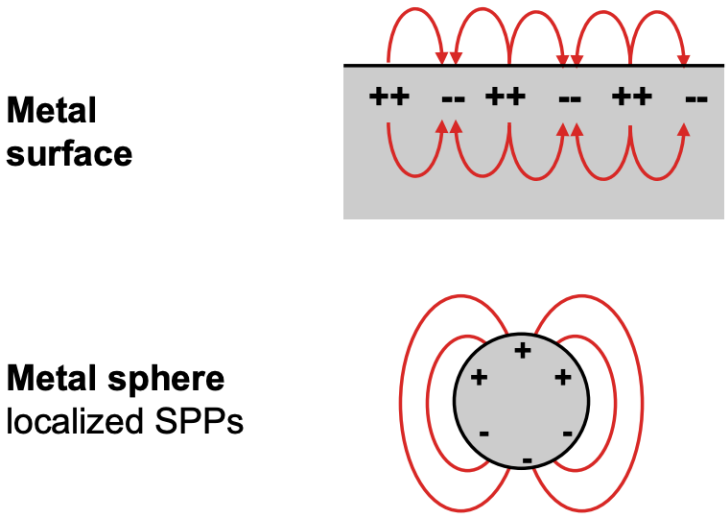


**Figure 1.6:** Graphic depicting different types of plasmons from a lecture posted by ETH Zurich [6]. Top: Charge configuration for a surface plasmon polariton (SPP) for a large metal surface. Bottom: Charge configuration for a localized surface plasmon polariton, which refers to the restriction of the charge to a small geometry. These localized SPPs are excited when the nanoparticles are comparable to the wavelength of light.

The dispersion relation for a surface plasmon polariton is

$$k_x = \frac{\omega}{c}\sqrt{\frac{\epsilon 1 \epsilon 2}{\epsilon 1 + \epsilon 2}} \tag{1.2}$$

where $k_x$ is the propagation constant, $\omega$ is the angular frequency of the surface plasmon, c is the speed of light, $\epsilon 1$ is the dielectric function of the metal, and $\epsilon 2$ is the dielectric function of the dielectric. Dielectric functions describe a material's dielectric properties for different wavelengths of incident radiation. The dispersion relation for SPPs can also be shown graphically as in figure 1.7

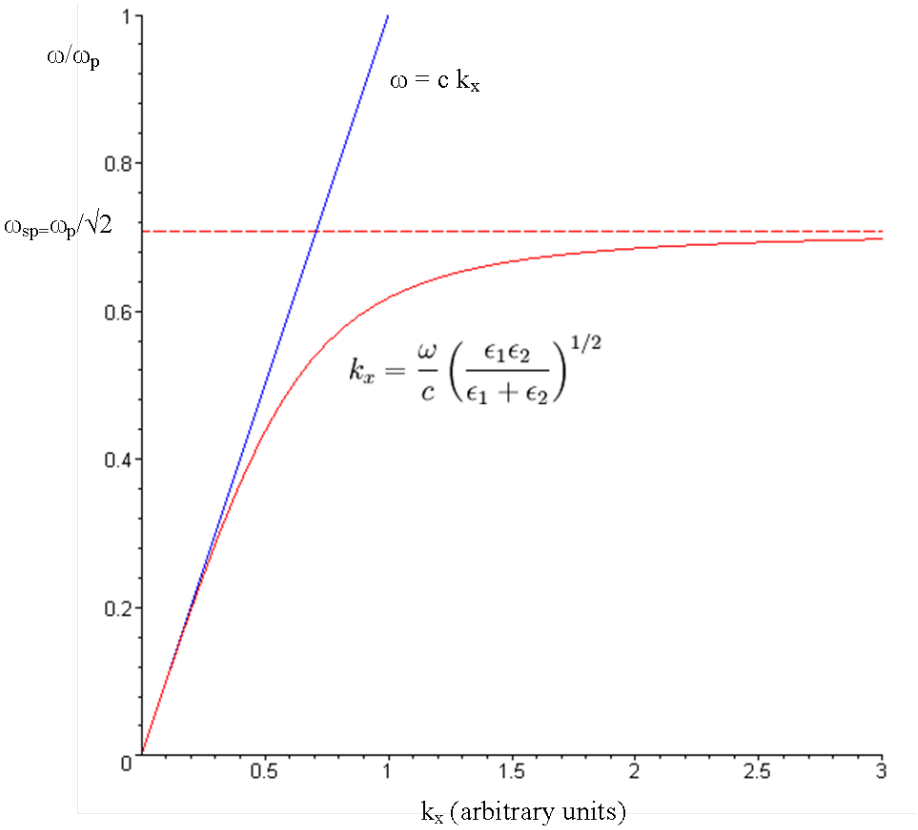


**Figure 1.7:** Dispersion relation for an SPP created by wiki user ScottTParker [7]. For high $k_x$, the frequency of the SPP approaches the surface plasmon frequency $\omega_{sp}$ which is equal to the plasma frequency $\omega_p$ over $\sqrt{2}$. The plasma frequency is a property of materials that depends on the number density of charge carriers and their effective mass within the material. At $\omega_{sp}$, the SPPs are on resonance and become standing waves because the phase velocity, $\frac{\omega}{k}$, approaches zero for large values of $k_x$. As the use of plasmonic MZIs require propagating waves, they must be operated off resonance at a value of $\omega$ slightly lower than $\omega_{sp}$.

As seen here, the propagation of a surface plasmon polariton is dependent only on the materials and the incident wavelength of light. SPPs are therefore independent of the object's size. In contrast, localized surface plasmons are highly dependent on the size of the particle. [8]

The voltage-length product, a key parameter used to characterize EO device, shows how the use of plasmonics allows for drastic size reduction. For a waveguide of length L, the voltage needed to shift the phase of light by half a wavelength is $U_\pi$. Thus the voltage length product is $U_\pi * L$ which can be expressed in terms of material and device parameters:

$$U_\pi * L = w\lambda/(n^3 * r_{33} * \Gamma), \tag{1.3}$$

where $\lambda$ is the vacuum wavelength of the optical signal, $w$ is the distance between the rails, $n$ is the index of refraction, and $\Gamma$ is the field interaction factor which characterizes how strongly the optical fields and radio frequency fields overlap in the material. [2]. Minimizing $U_\pi L$ allows one to reduce either the voltage or the length of the waveguide, so maximizing n, $r_{33}$, and $\Gamma$ will scale down these EO devices. The field interaction factor $\Gamma$ ranges from 0 to 1: 0 if the two fields have exactly no overlap, 1 if the two fields are confined to the exact same space and have equal phase. Equation 1.3 is for a purely photonic modulator, but it serves as a simple model to show how these material parameters affect device length and necessary voltage. The equation for plasmonic modulators is very similar, takes into account the slow propagation of the SPP.

$$U_\pi * L = w\lambda/(n^2 * r_{33} * \Gamma_E * n_{slow}), \tag{1.4}$$

where $\Gamma_E$ denotes the field energy interaction factor and $n_{slow}$ reflects the effect of reduced energy velocity in plasmonic slot waveguides [9]. Plasmonic devices specifically reduce $\Gamma_E$ by confining the optical fields to the slot of the waveguide, which is where the RF fields lie. This spatial confinement increases the overlap between the two fields, thereby raising $\Gamma_E$. See section 1.4 for a discussion on how to raise this factor through phase matching by using organics.

The field confinement along with a high electro-optic coeffiecient $r_{33}$ and small slot width $w$ result in a drastic reduction in size, as shown in figure 1.8

Combining plasmonics and organic electro-optics, the researchers in the Robinson Group at the University of Washington and their collaborators at ETH Zurich have succeeded in developing and fabricating such electro-optic modulators on the micron scale. An image of a single arm of their modulator is shown in figure 1.9. These modulators are currently stand-alone devices, and have yet to be densely integrated on an IC.

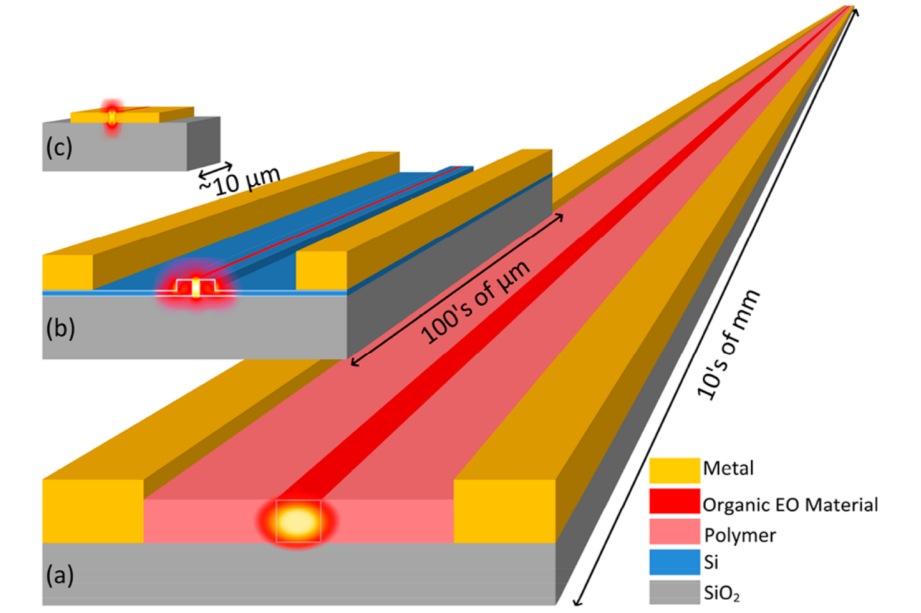


**Figure 1.8:** Length comparison of a) photonic, b) silicon-organic, and c) plasmonic devices from Heni et al. [9]. The photonic device has the drive voltage applied across the two gold rails, the voltage drop occurs across the entire distance between the rails. These photonic devices are meant to compete with conventional fiber-optic modulators, not with silicon-organic and plasmonic devices which have the goal of chip-integration. The silicon-organic device has most of the voltage drop across the slot that contains the OEO material, resulting in strong overlap between the optical and RF fields. Plasmonic-organic devices modulate the phase of a specific type of surface wave, the surface plasmon polariton (SPP) which is described below.

Plasmonic-organic hybrid waveguides have applications outside of interferometers. For example, Salamin et al. explore the possibility of using them as plasmonic mixers for direct wireless-to-optic conversion, bypassing the need for high speed electronics usually needed for such a conversion [10].

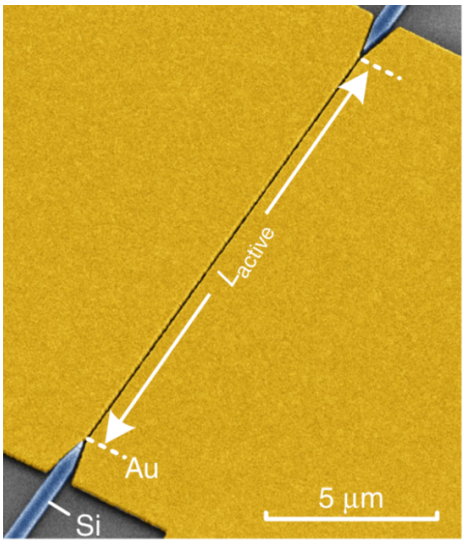


**Figure 1.9:** Scanning electron microscope image of a single plasmonic waveguide (before OEO material is applied) [4].

## 1.4 Chromophores

The previous section covered how plasmonics differs from photonics, and how these devices work through the use of the Pockels effect. This section will focus on the organic component of plasmonic-organic electro-optic devices. The term organic in this context refers to the polymers used as the electro-optic material within the slot of the waveguide, which have carbon atoms in their molecular structure. Not all materials that exhibit the Pockels effect are organic; in fact, inorganic electro-optics materials, such as lithium niobate, were preferred over organic materials for a long time (and still are, for discrete devices), as organics exhibited lower electro-optic activity and also had issues with optical loss, thermal stability, and photochemical stability [11]. It was in the late 90s and early 2000s that organic materials were improved to the point they could be considered competitive against inorganic crystals. The need for high electro-optic activity can be seen using the voltage-length product 1.4 discussed in section 1.3. The voltage-length product is inversely proportional to the electro-optic coefficient $r_{33}$, which quantifies the magnitude of the shift in index of refraction in response to an applied electric field. A large $r_{33}$ reduces the voltage-length product, so recent research into organics has been the development of materials

with extremely high EO coefficients. Unfortunately, the organic materials with high EO coefficients also tend to have large complex indices of refraction. This results in large energy losses in the SPPs as they propagate along waveguide, reducing the length that the wave can cover before dying out. Thus, there is a clear need to balance high EO activity with energy loss when selecting a material for use in these waveguides.

With that said, there are currently inorganic crystals such as $BaTiO_3$ which have higher EO coefficients than the organic materials used in these waveguides, so why not use these inorganics instead? There actually have been devices fabricated using $BaTiO_3$ as the EO material, but they end up having relatively high voltage-length products (a parameter we want to minimize) due to the complexity of the growth process of crystal, which can only be used with rather simple phase shifter structures. [12] Also, crystalline materials tend to have much higher dielectric constants for radio frequencies than for optical frequencies, resulting in a mismatch between the phase velocities of the electrical and optical signals. As mentioned towards the end of section 1.3, the field energy interaction parameter $\Gamma_E$ decreases when the two signals overlap poorly, which is the case with EO crystals. Additionally, $BaTiO_3$ specifically has a low Curie temperature, around 120°C, resulting in poor thermal stability for these devices.

There are two main reasons for using organics: the ease of material processing and the phase-matching of the optical and RF fields. Organics are able to strike this important balance between material parameters and applicability– they are easily integrated with a variety of device structures and have considerable EO figures of merit, resulting in strong overall device performance.

On the other hand, organic materials do not have such a mismatch in their dielectric responses to optical and radio frequency radiation. Thus, the optical and electrical fields have greater overlap, resulting in a higher $\Gamma_E$.

## 1.5 The Project

Electro-optic modulators on the micron scale have already been developed and fabricated by the members of the Robinson group and their collaborators at ETH Zurich, as shown in figure 1.9. The Robinson group does research and fabrication of the organic polymers used in the EO devices which are then fabricated at ETH Zurich. The next step is to create a computational elec-

trodynamics model of these devices in order to test various modifications in device geometry, material selection, additional cladding layers, etc. This computational model would allow researchers to experiment with different device parameters in order to optimize these device's performance without having to fabricate and validate prototype devices. The Masiello group at the University of Washington does theory-centric research and electrodynamics simulations, so a joint project between the Robinson and Masiello groups was created in order to develop a computational model of these EO modulators. This thesis will cover the application of the techniques and software of the Masiello group in order to model the devices studied and developed by the Robinson group. Specifically, simplified models of the devices were created using the electrodynamics software used by the Masiello group, the Discrete Dipole Approximation (DDA), in order to validate whether or not DDA would be a suitable software to use for a full waveguide simulation. This validation is carried out by comparing electric field results of the simplified simulations to what is physically expected. Once these simpler models make physical sense, it is possible to extend them to more complex models. The following chapters cover the operation of DDA, the simplified two-rail model, the results of those simplified simulations, and the future work of this project.

# Chapter 2

# Discrete Dipole Approximation

## 2.1 DDA Validation

One software option for creating a computational model of these electro-optic modulators is the Discrete Dipole Approximation (DDA). DDA was originally developed by Purcell and Pennypacker for "computing scattering and absorption by a particle of arbitrary shape." [13] The software was later adapted by Draine to glean information about the geometry of interstellar dust grains. The software's ability to deal with arbitrary geometries was useful as analytical models of the time generally dealt with spherical particles. The Masiello group at the University of Washington has found the software useful for studying nanostructures and developing analytical models. In addition to handling arbitrary geometries well, DDA is being considered for this application as it is able to accurately simulate the dielectric properties of organic materials using Monte Carlo simulations. The following chapter describes the operation of DDA, as well as some of its advantages and disadvantages.

## 2.2 How it Works

The Discrete Dipole Approximation uses an array of polarizable points, provided by the user, to approximate a continuum target–for this project, a waveguide.

When a simulation is run, this array of points is hit with an electromagnetic plane wave (propagating in the x direction) of certain wavelengths that the user provides. The points become polarized by the oscillating plane wave, gaining their own dipole moments from the excitation. Each dipole moment creates its own electric field, which then affect the surrounding dipoles, allowing the points to interact with each other. Of course, as this array is meant to approximate a finite, continuum target, the closer together the dipoles are spaced (i.e. the higher dipole density), the more accurate the solutions. Adding more dipoles also increases the simulation's complexity, resulting in longer run times. For the following simulations, a dipole spacing of 5 nm was used to balance run times with accuracy. Even with this balance, simulations of full waveguides only a few hundred nanometers in length take a day or more to compute. As these waveguides are several microns long, ideally these simulations would use periodic boundary conditions along the length of the model to avoid week-long run times. Periodic boundary conditions are used in computational models to repeat a target along a given direction to approximate infinite length in that dimension. For the waveguide model, this would be the direction of propagation, the x direction. Unfortunately, DDA is only able to utilize periodic boundary conditions in the y and z directions, not the direction of propagation.

DDA is capable of running both scattering and electric field simulations. Scattering simulations provide information about how the target responds to different wavelengths of light. This spectrum can be used to identify potential resonance modes of the target, as discussed in the Results/Analysis chapter. DDA can also use the polarizations of the dipoles to solve Maxwell's equations at specified points, extracting the electric fields associated with those points. The general process of how these simulations are run is shown in figure 2.1.

## 2.3 General Process

### 2.3.1 Shape File

As described above in figure 2.1, the software needs to know what geometry it will be running for both the scattering and electric field simulations. This information can be given in either the ddscat.par file, in which you can specify one of the pre-coded geometries, or it can be given using an external shape file.

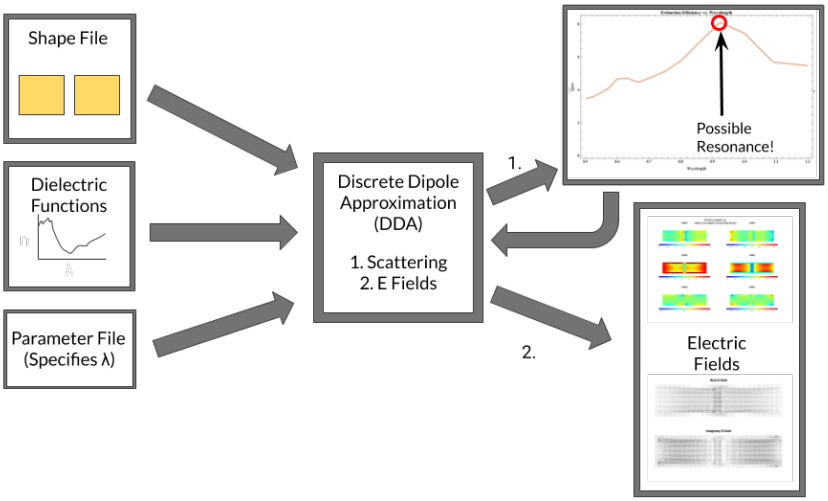


**Figure 2.1:** Graphical overview of simulation process. The user provides several input files to run both scattering and electric (E) field simulations. These include a shape file containing the target geometry, files containing dielectric functions for each material, and a parameter file specifying the incident wavelength, the spacing between dipoles, and whether or not to run an E field simulation. DDA takes these text files, and runs either a scattering simulation or an E field simulation based on the parameter file. Generally, the scattering simulation is run first. This outputs text files which describe the scattering, absorption, and extinction spectra, which can be used to identify potential resonances for the target. The user can then go back to the parameter file and choose specific wavelengths for which to run electric field simulations. This outputs a binary file which can be used to calculate the electric fields at points that are specified in another text file called ddfield.in.

As the geometry of these EO devices are not one of the pre-coded standards, it was necessary to create and provide the shape file. Fortran code created by Elliot Beutler, a graduate student at the University of Washington, was modified from its original function of generating shape files for ellipses to generating shape files for plasmonic-organic waveguides.

The shape file contains information about the location of each dipole, and it also has information about the dielectric properties of the continuum target it is meant to approximate. The process for generating and plotting these shape

files is described in figure 2.2

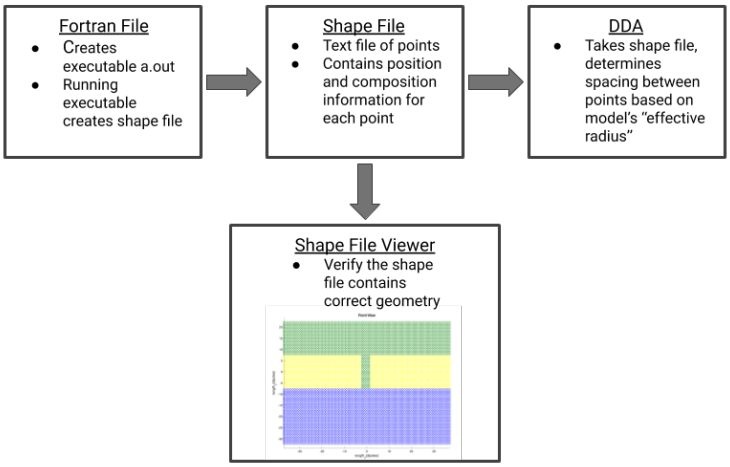


**Figure 2.2:** Graphical overview of shape file making process. First, a Fortran file is compiled to create the executable a.out, which when ran creates a text file containing the total number of dipoles, as well as those dipoles' positions and compositions. This shape file can be viewed using a MatLab script which was originally created by Elliot Beutler, and was further developed to use color to identify the different material compositions. DDA then takes this shape file and uses the effective radius specified in the ddscat.par file to determine the spacing between dipoles.

Each dipole is assigned six numbers corresponding to its dielectric functions in the x, y, and z directions in addition to its position in cartesian coordinates. These numbers are not actually dielectric values, they are simply markers meant to allow the software to distinguish which dielectric function should be assigned to each dipole. For example, if the shape file has 1 1 1 for the x, y, and z directions, then the software will look to the ddscat.par file to see which dielectric function corresponds to the number 1. This allows for the use of birefringent materials in the simulation, as it is possible to assign different dielectric functions to different coordinate directions (i.e. 1 2 3 instead of 1 1 1). A dielectric function specifies the real and imaginary indices of refraction with respect to the incident wavelength of EM waves. As these indices are dependent on wavelength, it is important that the software know how each material behaves when

subjected to the frequencies of light the user wants to be working with. These dielectric functions can be determined experimentally, and there is also an online database, https://refractiveindex.info/, containing dielectric information on a number of materials. An example of gold's dielectric function is shown in figure 2.3

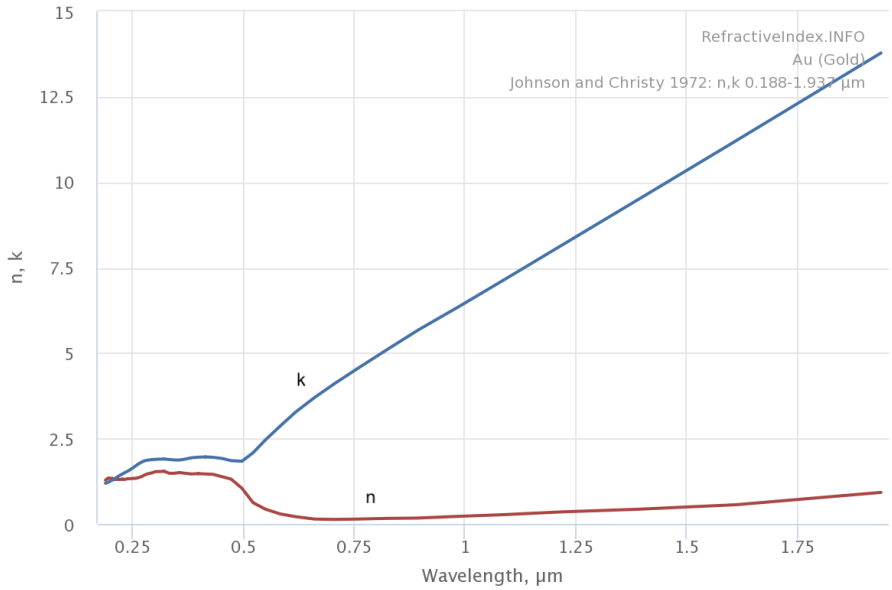


**Figure 2.3:** Dielectric function for gold taken from the online database https://refractiveindex.info/. This specific data is for wavelengths from 188 nm to 1937 nm, which covers the range of optical frequencies these devices will use. The blue corresponds to the imaginary part of the refractive index, k, and the red corresponds to the real part, n.

The dielectric functions for the $SiO_2$ substrate and Si grating tip were found using this website. Dielectric data for each of the materials is contained in separate files that can be referenced by the software. One important thing to note is that since these dielectric function files are discrete and finite, the software interpolates between and extrapolates from the provided data points to work with the exact wavelengths the user specifies, it is therefore crucial to use units of microns for specifying the wavelengths when creating dielectric functions, as the software will operate regardless of whether those wavelengths

are inside are outside the provided data range.

### 2.3.2 Parameter File

While the shape file and dielectric function files have information about the geometry and composition of the object, the parameter file ddscat.par tells the software where to find those files. Additionally, this parameter file specifies the wavelengths of incident light, the orientation of the object with respect to the incident light, whether or not to use periodic boundary conditions, the size of the object, the max number of iterations the algorithm should go through, and what kind of calculation (scattering or electric field) is to be run.

## 2.4 Scattering Outputs

Scattering calculations output several files. The most relevant ones are ddscat.log and qtable. The ddscat.log file keeps a record of how the software is running. It records whether or not the software finds the dielectric function that the ddscat.par file refers to, whether or not a shape file has been entered, and it keeps track of the number of iterations of the algorithm were needed to complete the calculation. If any of these files are unable to be found, or the number of max iterations is exceeded, the software stops running and outputs the partially completed qtable file, along with a description of the error that was encountered in the ddscat.log file. The log file is important to check when a qtable file comes out empty or incomplete, as it often has the information needed to effectively troubleshoot.

The qtable file is where the results of the scattering calculations are stored. This includes absorption, scattering, and extinction efficiencies for each incident wavelength. These efficiency values can be easily plotted against wavelength using a Mathematica notebook I developed, which allows for easy visualization of the spectra to identify local maxima and minima. The use of these spectra is described in detail in the Results/Analysis Chapter.

## 2.5 Electric Field Calculation Outputs

When an electric field calculation is run, the software outputs polarization files with file type *.pol1. These are binary files containing information about the

polarizations of each dipole. In order to find electric fields, it is necessary to create another input file, ddfield.in, which specifies the points at which the electric fields should be calculated. Using the ddfield executable, DDA uses the polarization file to solve Maxwell's equations at each point specified in ddfield.in, outputting electric field files with file type *.E. These are text files containing real and imaginary electric field components for the x, y, and z directions. These files can be plotted in MatLab in a variety of ways, depending on what the data is meant for. See Chapter 3 for examples.

## 2.6 Simplified Model

In order to verify that DDA is able to accurately simulate these plasmonic structures, it is necessary to run simplified models. A simplified two rail model with no substrate and no EO material was developed in order to test whether or not the software outputs physically expected results. The rail models used are much shorter in length than the actual waveguides, as they were originally meant to be used as unit cells for periodic boundary conditions. As mentioned in section 2.2, DDA is unable to utilize periodic boundary conditions along the axis of propagation, so instead these models were used to determine if rails with lengths shorter than the incident wavelength of light would accurately approximate a much longer model, and whether or not the simulations output physically expected results. In the following section, it was determined that while the short-rail simulations do appear to give physically reasonable results, they are not able to approximate longer rail models.

# Chapter 3

# Results/Analysis

## 3.1 Overview

The final goal of this project is to develop a computer model for plasmonic-organic hybrid waveguides, to allow researchers to explore new areas for optimization without the time and budget constraints of fabricating and validating prototypes. As part of that overarching goal, the research covered in this thesis serves as an investigation into the viability of the Discrete Dipole Approximation (DDA) as the electrodynamics software for this computer model. A basic model involving two gold rails was developed to lay the groundwork for this study. The purpose of this simplified model is to verify that DDA produces physically expected results, which we confirm by observing the model's dependence on wavelength and rail length in the direction of propagation before moving to more complex and computationally expensive models. These simulations demonstrate that the code needed to run each step in the process of using DDA has been developed successfully.

## 3.2 Length Dependence

As the length of these simulated rails was varied, it was found that the electric field profiles show a clear length dependence, which is consistent with exciting localized surface plasmons for each of the rails. Discussion on this will follow the model's explanation.

During the course of this project, it was discovered that DDA does not support periodic boundary conditions (PBCs) in the direction of light propagation, which is fixed by the software as the +x direction. PBCs are useful for when the object to be modeled is extremely long in one or two directions, and they work by repeating a target unit cell (TUC) along a prescribed axis. As the waveguides used in Mach-Zehnder Interferometer (MZI) devices are long in that dimension in comparison to their widths, it is unfortunate that PBCs cannot be used to represent this in DDA simulations. Instead, it is necessary to physically extend the geometry, which adds to computation time and expense.

Before the issue with PBCs had been discovered, a TUC consisting of two gold rectangular prisms meant to approximate the rails was created. These rails each had dimensions 160 nm, 350 nm, and 150 nm in the x, y, and z directions respectively, as shown in the figure below.

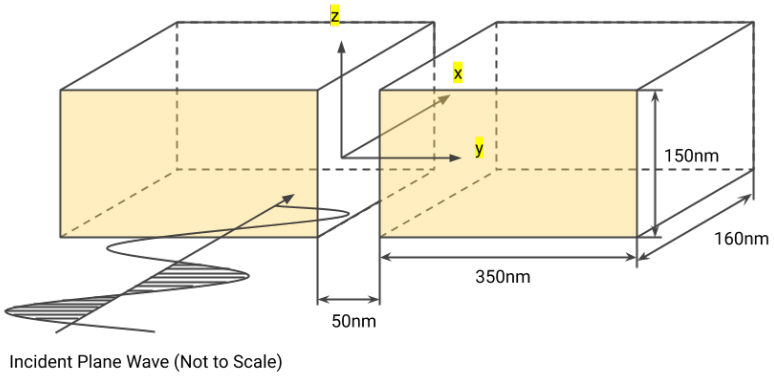


**Figure 3.1:** Diagram of two 160 nm long gold rails with a slot width of 50 nm. The oscillating wave indicates incoming plane waves (which are uniform in the y-z plane) that are propagating in the +x direction and are polarized in the y-direction. The wave shown in the figure is not to scale, as the actual optical-IR wavelengths (400 nm - 1200 nm) will be much longer than shown.

An additional shape file with the same y and z dimensions but twice as long in x was created to see how rail length changes the response of the model. These two geometries had electric field calculations run with an incident wavelength of

675 nm. As discussed in Chapter 2, the polarization file can be used to calculate the electric field at any prescribed x, y, z coordinate.

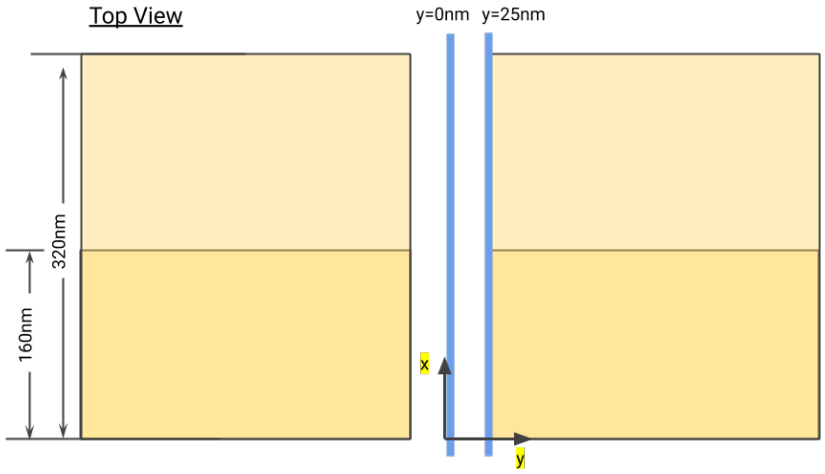


**Figure 3.2:** Top-down view demonstrating how the different length rails are positioned in their respective models.The subsequent analysis focuses on the electric field along lines at (y = 0 nm, z = 0 nm) and (y = 25 nm, z = 0 nm), as indicated in blue. The dark gold corresponds to the 160 nm long rails, and the lighter gold is to show the remaining half of the 320 nm long rails that does not overlap with the 160 nm rails.

The results of these simulations along two probe lines at z = 0 nm are shown in Figure 3.3. As the largest electric fields seen were in the direction of the incident plane wave polarization, only the y-component of the electric fields created by the excitations of the rails is shown.

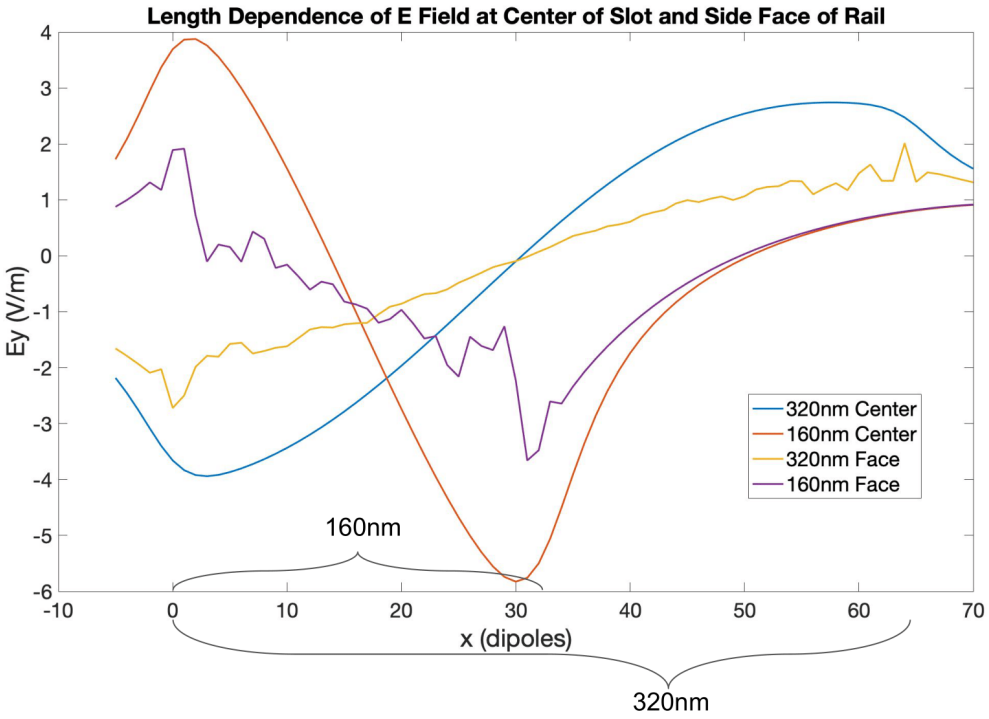


**Figure 3.3:** Results of DDA simulation, with the real part of the electric field's y-component plotted as a function of length through the waveguide. Spacing between dipoles for this simulation is 5 nm, so 32 dipoles in x corresponds to 160 nm, and 64 dipoles corresponds to 320 nm, as indicated. Data for both 160 nm and 320 nm long rail simulations are included in this plot. The probe lines are taken at z = 0 nm, for two different y values: 0 nm and 25 nm, which correspond to the center of the slot and the middle of a face, respectively.

Note that for the 160 nm rails, the electric field in the middle of the slot undergoes a full oscillation, going from max in the positive y direction at the front of the rails, to max in the negative y direction at the end of the rails, and then decaying once beyond the length of the rails. In comparison, the corresponding probe for 320 nm long rails shows an electric field going from a max in the negative y direction at the front, to a max in the positive y direction at the end. There's a slight taper at the end that may indicate exponential decay, much like with the 160 nm rails. This result is interesting, because the wavelengths of these oscillations seem to match the length of the rails, even

though the incident wavelength (675 nm) is much longer than either of the two.

The length-dependence of these electric field profiles can be interpreted as evidence of localized surface plasmon resonance (LSPR). LSPRs are collective oscillations of the electrons of a nanoparticle, which are excited when the nanoparticles are similar to or smaller than the incident wavelength. In these simulations, the incident wavelength is longer than the rails. Unlike surface plasmon polaritons which have resonant frequencies independent of length, LSPRs depend on the geometry of the conductive nanoparticles. [8]

These simulations produce physically reasonable results, as the rails are much smaller than the wavelength of incoming light, making the rails essentially large nanoparticles. Experimenting with longer and longer rails will be interesting, as eventually this localized surface plasmon excitation should become a surface plasmon polariton. By increasing the rail length, the electric fields in the middle section of the rails, away from the front and back faces, should begin to converge. As the rails get longer, there should come a point when the fields stop changing appreciably. Finding the minimum lengths of rails required for this convergence is crucial for minimizing computation time and expense before making the simulations more complex, as including the substrates and dielectrics in the geometry will only compound the extra computation time.

## 3.3 Wavelength Dependence

The other parameter being investigated was the wavelength of incident light. As discussed in Chapter 2, the process for running DDA simulations involved running scattering spectrum calculations for the geometries. From this spectrum, it should be possible to identify different resonant wavelengths.

Results of the scattering simulations are shown in figure 3.4. The extinction, absorption, and scattering efficiencies are plotted as a function of wavelength, where extinction efficiency describes the total effect on a medium on radiation passing through it. Specifically, extinction efficiency is defined as the sum of absorption and scattering efficiencies. [14]. These data suggest two resonances, one at a wavelength two times the length of the rail ($\sim$600 nm), and the other at a wavelength three times the length of the rail ($\sim$900 nm).

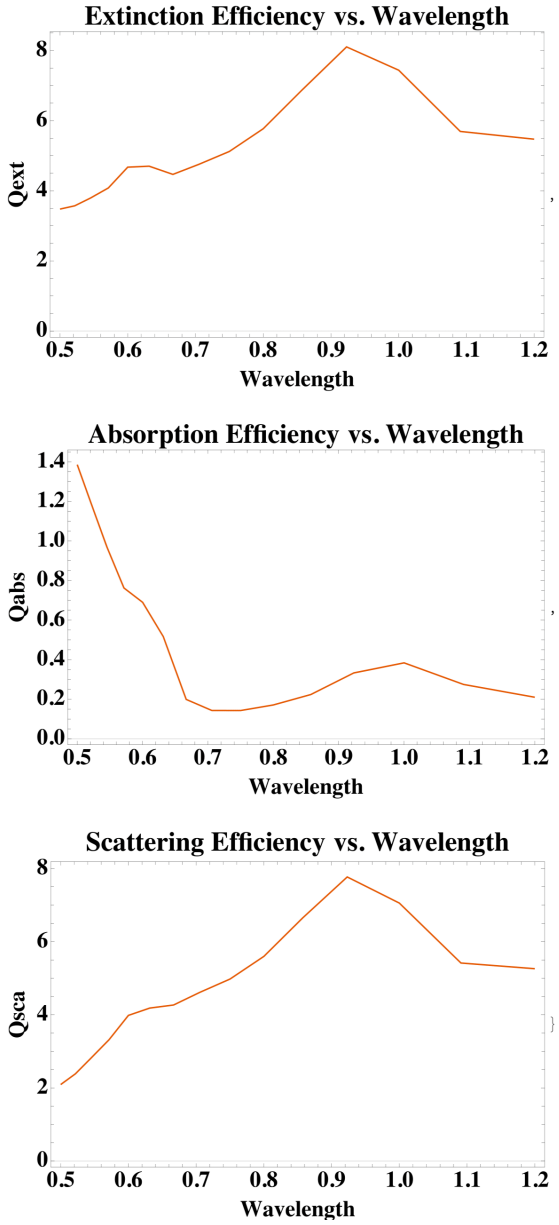


**Figure 3.4:** Extinction, absorption, and scattering efficiency spectra for 320 nm long gold rails. The wavelength is in units of $\mu$m. The peak at 0.923 $\mu$m (923 nm) is a potential resonance, so an electric field calculation was carried out at that wavelength.

Only 15 wavelengths were run in a range from 500 nm to 1200 nm, resulting in a wavelength spacing of about 47 nm. More exact positions of these peaks can be found by running the spectrum with closer-spaced wavelengths. If these resonances are indeed at two and three times the length of the rails, it is possible that resonances occur at every integer multiple of the rail length.

Clearly, there is a maximum in the extinction spectrum around 923 nm. This maximum in the spectrum can be indicative of a plasmon resonance, so electric field calculations were carried out with incident wavelengths of 923 nm and 675 nm, where the extinction spectrum has a local maximum and minimum, respectively. Electric field magnitudes for simulations off-resonance and on-resonance are shown in figure 3.5.

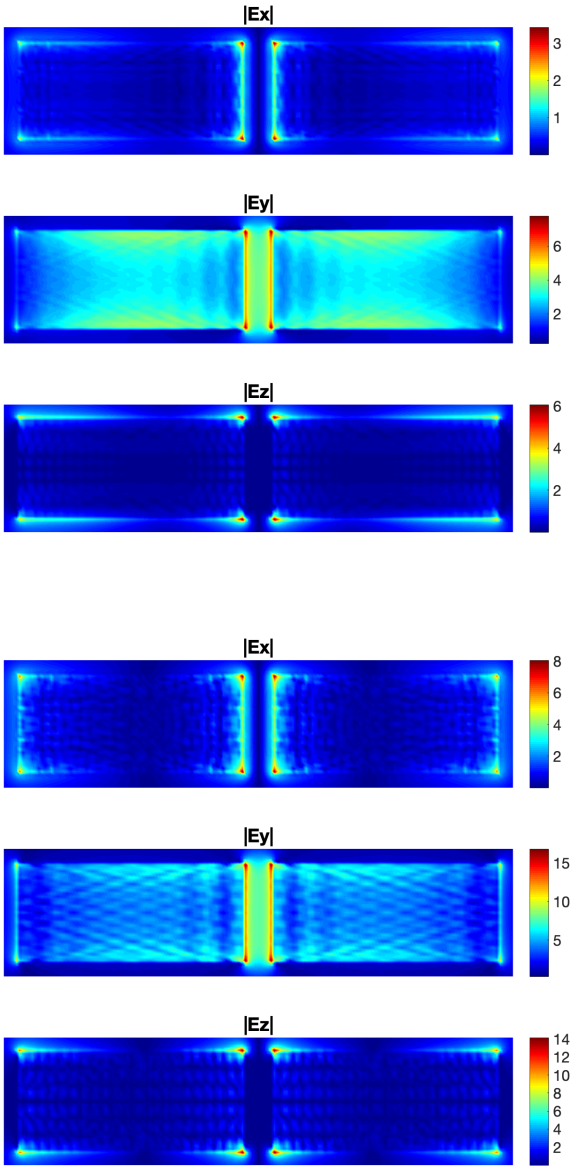


**Figure 3.5:** These are y-z cross sections at the front face of the 320 nm rails. These are both electric field magnitude plots $(real^2 + imaginary^2)^{1/2}$. The top three cross sections are the x, y, and z components of the electric field for an incident wavelength of 675 nm, and the bottom three are for an incident wavelength of 923 nm.

Electric field magnitudes are larger for an incident wavelength of 923 nm than 675 nm, corresponding to the existence of a resonance near 923 nm. Specifically, the magnitudes of the electric field components are larger at resonance than off resonance, as expected for higher magnitude oscillations at resonance.

To provide further confirmation of higher electric field magnitudes on resonance, cross sections at various x positions are compared in figure 3.6. Five y-z cross sections were taken from front to back, with spacings of 80 nm in between.

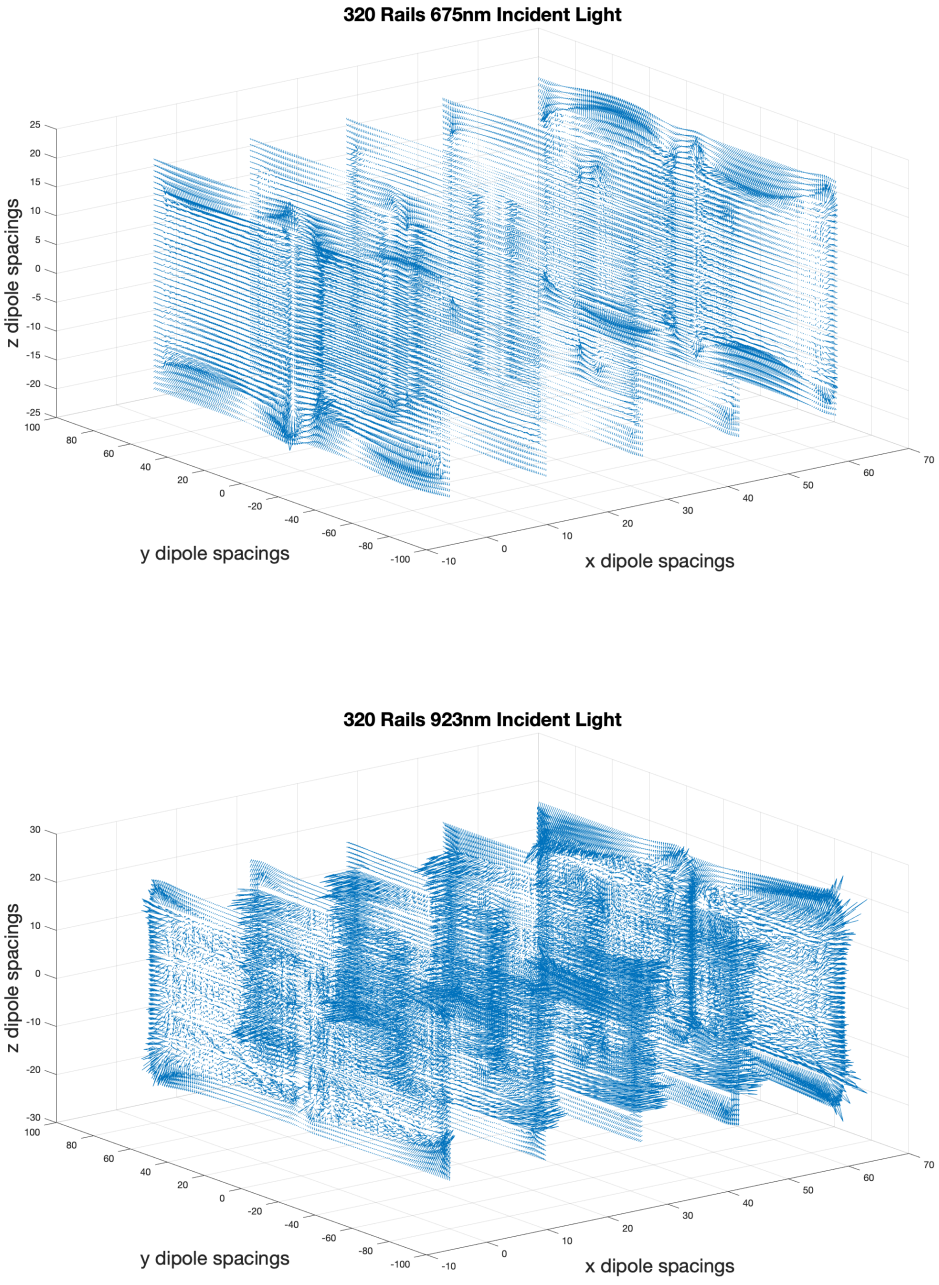


**Figure 3.6:** 3D vector field plot demonstrating the five cross sections for 675 nm (top) and 923 nm (bottom) incident light.

As the incident light has two different wavelengths, it is inappropriate to compare cross sections with common x values. Instead, the maximum magnitudes of each electric field component from each cross section will be compared between the two simulations. The maximum values of each electric field component are extracted, and the largest of those are collected in the final row, as shown in table 3.1.

| 320 nm Rails, 675 nm Incident Wavelength | | | | | |
|---|---|---|---|---|---|
| E-Field Components | CS1 | CS2 | CS3 | CS4 | CS5 |
| Max $\|E_x\|$ (V/m) | 3.4357 | 2.3843 | 1.8361 | 2.8001 | 4.1217 |
| Max $\|E_y\|$ (V/m) | **7.79** | **3.403** | 2.8454 | **3.1817** | **8.6991** |
| Max $\|E_z\|$ (V/m) | 6.0576 | 2.6433 | **2.9581** | 1.9289 | 7.4286 |
| Largest of Each CS | **7.79** | **3.403** | **2.9581** | **3.1817** | **8.6991** |
| 320 nm Rails, 923 nm Incident Wavelength | | | | | |
| E-Field Components | CS1 | CS2 | CS3 | CS4 | CS5 |
| Max $\|E_x\|$ (V/m) | 8.0619 | **8.9838** | **11.1851** | 9.9598 | 8.9671 |
| Max $\|E_y\|$ (V/m) | **16.8231** | 8.477 | 2.9807 | **10.041** | **19.118** |
| Max $\|E_z\|$ (V/m) | 14.1567 | 6.5978 | 1.951 | 6.7533 | 15.2252 |
| Largest of Each CS | **16.8231** | **8.9838** | **11.1851** | **10.041** | **19.118** |

**Table 3.1:** Maximum electric field components for each cross section (CS). The largest electric field value for each cross section is in bold.

It is clear from these results that the electric field magnitudes are stronger for the 923 nm incident wavelength. This is evidence that a peak in the scattering spectrum does indeed correspond to larger electric field magnitudes. These strong excitations may indicate surface plasmon resonances.

In this chapter, simulations with various rail lengths and incident light wavelengths were shown to produce physically expected results. These results validate the simplified two-rail model, justifying the use of DDA to create more complex electrodynamics models with the goal of eventually simulating a plasmonic-organic waveguide.

It is clear from these results that the electric field magnitudes are stronger for the 923 nm incident wavelength. This is evidence that the scattering spectrum calculations do indeed correspond to larger electric field magnitudes. These strong excitations may indicate surface plasmon resonances.

The shape of these electric field profiles can be used to infer the potential charge configurations. An example of one such charge configuration is shown in figure 3.7.

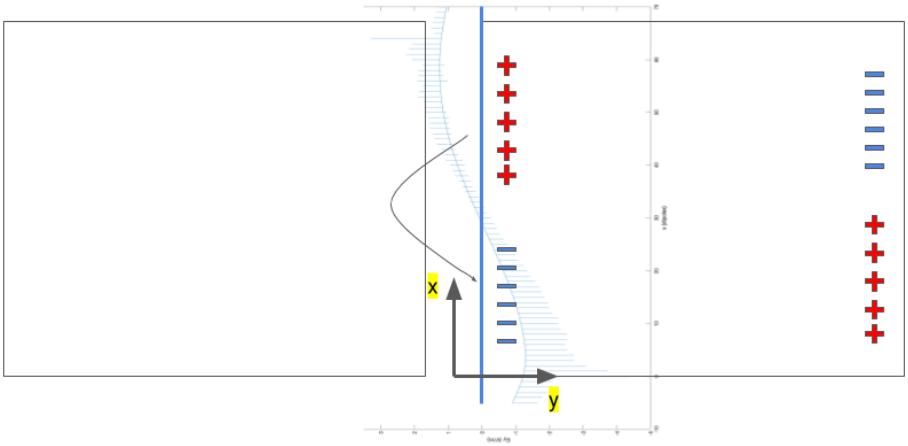


**Figure 3.7:** Potential charge configuration associated with the electric fields found at the left face of the right rail. The plot over which the charge configuration is superimposed is of the real y-component of the electric fields for an incident wavelength of 675 nm at all different z positions, ranging from beneath the rail to the top of the rail. The x and z components of the electric field were negligible in comparison. This charge configuration is that of a quadrupole, so this wavelength might be near a quadrupole resonance for each rail.

## 3.4 Overview

In this chapter, simulations with various rail lengths and incident light wavelengths were shown to produce physically expected results. These results validate the simplified two-rail model, justifying the use of DDA to create more complex electrodynamics models with the goal of eventually simulating a plasmonic-organic waveguide.

# Chapter 4

# Conclusion/Future Work

## 4.1 Recap

The end goal of this joint project between the Robinson and Masiello research groups was to develop a computer model of these electro-optic modulators that would allow research scientists to experiment with different aspects of the modulators, such as device geometry and composition, without having to fabricate and validate every experimental device. This would provide researchers with a low-cost, efficient method to identify possible paths for optimization.

## 4.2 Future Work

The Discrete Dipole Approximation was chosen initially for the electrodynamics software because of its ability to deal with arbitrary geometries, anisotropic dielectric functions, and its compatibility with Monte Carlo simulations. Over the course of this project, it was discovered that this software does not support periodic boundary conditions (PBCs) in the direction of propagation, so it was eventually concluded that transitioning to Lumerical, an alternate software which is able to do propagation-direction PBCs, would be the next step in the simulation process. Lumerical simulations are generally more intuitive and less work intensive than DDA simulations, as users interact with the software through a graphical user interface as opposed to through their computer's terminal. There are still potential uses for DDA simulations: for corroborat-

ing Lumerical results, and more detailed simulations. As seen in the previous chapter, the dependence of the electric fields on the rail length and incident wavelength suggest the DDA simulations are producing physically reasonable results. However, there are a few refinements to the model that need to be implemented in order for those simulations to be used for actual waveguides. In order to approximate the extreme length of the rails in comparison to the slot width, the model needs to be extended to the point of convergence. Additionally, the rails could potentially be made wider to better reflect the actual dimensions of these waveguides. Increasing the simulation's dipole density would provide more accurate results.These improvements are shown graphically in figure 4.1.

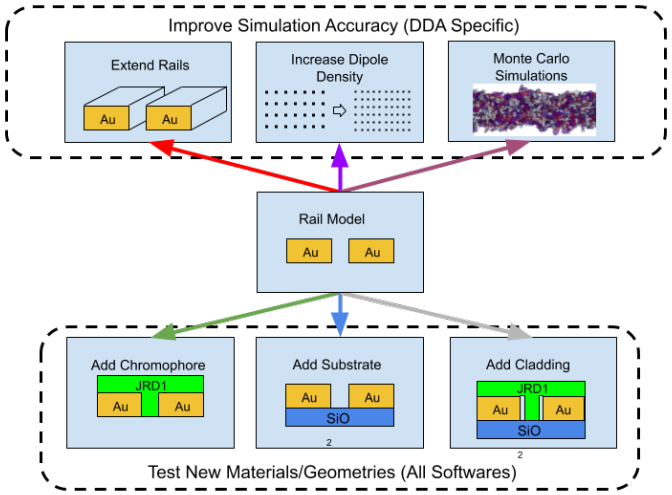


**Figure 4.1:** The basic model and proposed future work. There are specific improvements to the DDA model that can help increase the simulation accuracy, and there are general improvements to the model as a whole that will prove useful for other electrodynamics softwares as well. Image of Monte Carlo Simulation results from Johnson et. al. [2]

The third point for DDA specific simulation accuracy, the integration of Monte Carlo simulations is one of the reasons DDA was examined as an option in the first place. The chromophores are ordered using electrical poling, but there are interactions with the gold interface and general randomness in the poling that can be directly simulated using Monte Carlo methods. [2]

The results of the simulations conducted for this thesis show evidence that

DDA is able to produce physically expected results for short two gold rail models. This suggests DDA can be used for more complex simulations, including a full waveguide model, as long as the suggested changes are implemented.

# Bibliography


[1] N. Massa, "Fiber Optic Telecommunication," in *Fundamentals of Photonics*, University of Connecticut, 2000, pp. 293–347. [Online]. Available: https://pdfs.semanticscholar.org/19a3/d51ca70fee577a4636894f22c2dfd4ee65c7.pdf (visited on 11/02/2019).

[2] L. E. Johnson, D. L. Elder, A. A. Kocherzhenko, A. F. Tillack, C. M. Isborn, L. R. Dalton, and B. H. Robinson, "Poling-Induced Birefringence in OEO Materials Under Nanoscale Confinement," in *Organic and Hybrid Sensors and Bioelectronics XI*, vol. 10738, International Society for Optics and Photonics, Sep. 2018, 107381A. DOI: 10.1117/12.2321997. [Online]. Available: https://www.spiedigitallibrary.org/conference-proceedings-of-spie/10738/107381A/Poling-induced-birefringence-in-OEO-materials-under-nanoscale-confinement/10.1117/12.2321997.short (visited on 09/28/2019).

[3] A. Melikyan, L. Alloatti, A. Muslija, D. Hillerkuss, P. C. Schindler, J. Li, R. Palmer, D. Korn, S. Muehlbrandt, D. Van Thourhout, B. Chen, R. Dinu, M. Sommer, C. Koos, M. Kohl, W. Freude, and J. Leuthold, "High-Speed Plasmonic Phase Modulators," en, *Nature Photonics*, vol. 8, no. 3, pp. 229–233, Mar. 2014, ISSN: 1749-4893. DOI: 10.1038/nphoton.2014.9. [Online]. Available: https://www.nature.com/articles/nphoton.2014.9 (visited on 09/28/2019).

[4] W. Heni, Y. Fedoryshyn, B. Baeuerle, A. Josten, C. B. Hoessbacher, A. Messner, C. Haffner, T. Watanabe, Y. Salamin, U. Koch, D. L. Elder, L. R. Dalton, and J. Leuthold, "Plasmonic IQ Modulators With Attojoule Per Bit Electrical Energy Consumption," en, *Nature Communications*, vol. 10, no. 1, pp. 1–8, Apr. 2019, ISSN: 2041-1723. DOI: 10.1038/s41467-019-

09724-7. [Online]. Available: https://www.nature.com/articles/s41467-019-09724-7 (visited on 09/28/2019).

[5] L. Sun, P. Chen, and L. Lin, "Enhanced Molecular Spectroscopy via Localized Surface Plasmon Resonance," en, *Applications of Molecular Spectroscopy to Current Research in the Chemical and Biological Sciences*, Oct. 2016. DOI: 10.5772/64380. [Online]. Available: https://www.intechopen.com/books/applications-of-molecular-spectroscopy-to-current-research-in-the-chemical-and-biological-sciences/enhanced-molecular-spectroscopy-via-localized-surface-plasmon-resonance (visited on 12/22/2019).

[6] *Lecture 5: Plasmons*. [Online]. Available: https://www.photonics.ethz.ch/fileadmin/user_upload/Courses/NanoOptics/plasmons2.pdf.

[7] Scott T Parker, *Dispersion relationship*, 2007. [Online]. Available: https://en.wikipedia.org/wiki/Surface_plasmon_polariton#/media/File:Dispersion_Relationship.png.

[8] E. Petryayeva and U. J. Krull, "Localized Surface Plasmon Resonance: Nanostructures, Bioassays and Biosensing—A Review," en, *Analytica Chimica Acta*, vol. 706, no. 1, pp. 8–24, Nov. 2011, ISSN: 0003-2670. DOI: 10.1016/j.aca.2011.08.020. [Online]. Available: http://www.sciencedirect.com/science/article/pii/S0003267011011196 (visited on 12/09/2019).

[9] W. Heni, Y. Kutuvantavida, C. Haffner, H. Zwickel, C. Kieninger, S. Wolf, M. Lauermann, Y. Fedoryshyn, A. F. Tillack, L. E. Johnson, D. L. Elder, B. H. Robinson, W. Freude, C. Koos, J. Leuthold, and L. R. Dalton, "Silicon–Organic and Plasmonic–Organic Hybrid Photonics," *ACS Photonics*, vol. 4, no. 7, pp. 1576–1590, Jul. 2017. DOI: 10.1021/acsphotonics.7b00224. [Online]. Available: https://doi.org/10.1021/acsphotonics.7b00224 (visited on 09/28/2019).

[10] Y. Salamin, B. Baeuerle, W. Heni, F. C. Abrecht, A. Josten, Y. Fedoryshyn, C. Haffner, R. Bonjour, T. Watanabe, M. Burla, D. L. Elder, L. R. Dalton, and J. Leuthold, "Microwave Plasmonic Mixer in a Transparent Fibre–Wireless Link," en, *Nature Photonics*, vol. 12, no. 12, pp. 749–753, Dec. 2018, ISSN: 1749-4893. DOI: 10.1038/s41566-018-0281-6. [Online].

Available: https://www.nature.com/articles/s41566-018-0281-6 (visited on 09/28/2019).

[11] L. R. Dalton, P. A. Sullivan, and D. H. Bale, "Electric Field Poled Organic Electro-optic Materials: State of the Art and Future Prospects," *Chemical Reviews*, vol. 110, no. 1, pp. 25–55, Jan. 2010, ISSN: 0009-2665. DOI: 10.1021/cr9000429. [Online]. Available: https://doi.org/10.1021/cr9000429 (visited on 10/05/2019).

[12] C. Kieninger, Y. Kutuvantavida, D. L. Elder, S. Wolf, H. Zwickel, M. Blaicher, J. N. Kemal, M. Lauermann, S. Randel, W. Freude, L. R. Dalton, and C. Koos, "Ultra-high Electro-Optic Activity Demonstrated in a Silicon-Organic Hybrid Modulator," EN, *Optica*, vol. 5, no. 6, pp. 739–748, Jun. 2018, ISSN: 2334-2536. DOI: 10.1364/OPTICA.5.000739. [Online]. Available: https://www.osapublishing.org/optica/abstract.cfm?uri=optica-5-6-739 (visited on 09/28/2019).

[13] B. T. Draine, "The Discrete-Dipole Approximation and its Application to Interstellar Graphite Grains," en, *The Astrophysical Journal*, vol. 333, p. 848, Oct. 1988, ISSN: 0004-637X, 1538-4357. DOI: 10.1086/166795. [Online]. Available: http://adsabs.harvard.edu/doi/10.1086/166795 (visited on 10/06/2019).

[14] *Lecture 3: Optical Properties*. [Online]. Available: https://www.gfdl.noaa.gov/wp-content/uploads/files/user_files/pag/lecture2008/lecture3.pdf.